Remote Sensing of Environment 215 (2018) 97–108

Contents lists available at ScienceDirect

Remote Sensing of Environment

journal homepage: www.elsevier.com/locate/rse

Exploring the physiological information of Sun-induced chlorophyll fluorescence through radiative transfer model inversion

Marco Celesti[a,*], Christiaan van der Tol[b], Sergio Cogliati[a], Cinzia Panigada[a], Peiqi Yang[b], Francisco Pinto[c,d], Uwe Rascher[d], Franco Miglietta[e,f], Roberto Colombo[a], Micol Rossini[a]

[a] Remote Sensing of Environmental Dynamics Laboratory, Department of Earth and Environmental Sciences (DISAT), University of Milano-Bicocca, Piazza della Scienza 1, Milano 20126, Italy
[b] Faculty of Geo-Information Science and Earth Observation (ITC), University of Twente, P.O. Box 217, Enschede 7500 AE, The Netherlands
[c] Global Wheat Program, International Maize and Wheat Improvement Center (CIMMYT), Texcoco 56237, Mexico
[d] Institute of Bio- and Geosciences, IBG-2: Plant Sciences, Forschungszentrum Jülich GmbH, Jülich 52428, Germany
[e] Institute of Biometeorology, National Research Council (IBIMET-CNR), Via Caproni 8, Firenze 50145, Italy
[f] IMéRA, Institut de Recherches Avancés, Université Aix-Marseille, 2, Place Le Verrier, Marseille 13004, France

ARTICLE INFO

Keywords:
Sun-induced chlorophyll fluorescence
Fluorescence quantum yield
SCOPE
Numerical optimization
Plant status

ABSTRACT

A novel approach to characterize the physiological conditions of plants from hyperspectral remote sensing data through the numerical inversion of a light version of the SCOPE model is proposed. The combined retrieval of vegetation biochemical and biophysical parameters and Sun-induced chlorophyll fluorescence (*F*) was investigated exploiting high resolution spectral measurements in the visible and near-infrared spectral regions. First, the retrieval scheme was evaluated against a synthetic dataset. Then, it was applied to very high resolution (sub-nanometer) canopy level spectral measurements collected over a lawn treated with different doses of a herbicide (Chlorotoluron) known to instantaneously inhibit both Photochemical and Non-Photochemical Quenching (PQ and NPQ, respectively). For the first time the full spectrum of canopy *F*, the fluorescence quantum yield (Φ_F), as well as the main vegetation parameters that control light absorption and reabsorption, were retrieved concurrently using canopy-level high resolution apparent reflectance (ρ^*) spectra. The effects of pigment content, leaf/canopy structural properties and physiology were effectively discriminated. Their combined observation over time led to the recognition of dynamic patterns of stress adaptation and stress recovery. As a reference, *F* values obtained with the model inversion were compared to those retrieved with state of the art Spectral Fitting Methods (SFM) and SpecFit retrieval algorithms applied on field data. Φ_F retrieved from ρ^* was eventually compared with an independent biophysical model of photosynthesis and fluorescence. These results foster the use of repeated hyperspectral remote sensing observations together with radiative transfer and biochemical models for plant status monitoring.

1. Introduction

In the last years, Remote Sensing (RS) of Sun-induced chlorophyll fluorescence (*F*) emerged as a novel and promising scientific field for studying the dynamic behavior of photosynthesis (for a review of this topic see Meroni et al., 2009 and Porcar-Castell et al., 2014). *F* is a physical side product of light absorption that is emitted as an electromagnetic radiation in the red and far-red spectral regions (≈ 640 nm to 850 nm), and it is related to the energetic status of the photosystems.

The feasibility of consistent retrievals of *F* from ground based platforms (Rossini et al., 2016; Yang et al., 2015), Unmanned Aerial Vehicles (UAVs) (Garzonio et al., 2017; Zarco-Tejada et al., 2013), airplanes (Rascher et al., 2015; Rossini et al., 2015) and satellites (Cogliati et al., 2015; Guanter et al., 2015, 2010; Joiner et al., 2016) has been successfully investigated in the last years, with a strong impulse given by the activity supporting the Earth-Explorer 8 FLuorescence EXplorer (FLEX) satellite mission, of the European Space Agency (ESA), specifically intended for global-scale *F* retrieval from space (Drusch et al., 2017). Nevertheless, due to the concurrent influence of physiology, leaf and canopy structure, pigment concentration and weather conditions on *F* (Porcar-Castell et al., 2014; Verrelst et al., 2015b), it's unambiguous interpretation in terms of the quantification of vegetation photosynthesis and stress detection is a largely unsolved challenge. Several authors (*e.g.*, Damm et al., 2010, Guanter et al., 2014, Lee et al.,

* Corresponding author.
E-mail address: marco.celesti@unimib.it (M. Celesti).

https://doi.org/10.1016/j.rse.2018.05.013
Received 27 September 2017; Received in revised form 20 April 2018; Accepted 8 May 2018
Available online 15 June 2018

2013) exploited the conceptual scheme of the Light Use Efficiency (LUE) model, proposed by Monteith (1972) for the Gross Primary Production (GPP), to express F as:

$$F(\lambda) = PAR \times fAPAR \times \Phi_F(\lambda) \times f_{esc}(\lambda) \quad (1)$$

where PAR is the Photosynthetically Active Radiation, fAPAR is the fraction of PAR that is absorbed by vegetation (*i.e.*, the fraction of PAR that is transformed into Absorbed Photosynthetically Active Radiation (APAR)), $\Phi_F(\lambda)$ the fluorescence yield (also $LUE_F(\lambda)$, *i.e.*, the fraction of absorbed PAR emitted as fluorescence at wavelength λ), and $f_{esc}(\lambda)$ the "escape probability" (*i.e.*, the probability that an emitted fluorescence photon escapes the canopy in the direction of the sensor). These three processes together (*i.e.*, the absorption of light, the emission as fluorescence, and the escape of F from the canopy) determine the directional F flux emitted at the top of the canopy.

Given these definitions, the effective fluorescence quantum yield (Φ_F) can be defined as:

$$\Phi_F = \frac{F_{int}^{TOT}}{APAR} = \frac{\int_{640}^{850} \frac{F(\lambda)}{f_{esc}(\lambda)} d\lambda}{fAPAR \times PAR} \quad (2)$$

with F_{int}^{TOT} being the total emitted fluorescence by all photosystems in the leaves. Φ_F is modulated by changes in the physiological status of plants, and represents the fraction of absorbed energy that is not used for Photochemical (PQ) and Non-Photochemical Quenching (NPQ).

Although the potential of Φ_F to monitor photosynthesis has been demonstrated, it is not trivial to quantify it from canopy level measurements, with increasing complexity when moving from field to airborne and satellite observations. In particular: i) the calculation of F_{int}^{TOT} requires the retrieval of the full spectrum of emitted F, but only few attempts have been made so far to retrieve it at canopy level from ground measurements (Zhao et al., 2014; Liu et al., 2015), airborne (Cogliati et al., 2016) or simulated satellite data (Cogliati et al., 2015; Sabater et al., 2015); ii) it is not possible to directly measure f_{esc}; iii) the proper quantification of the components of APAR from RS is still challenging (cfr. Garbulsky et al., 2010, Gitelson and Gamon, 2015). Apart from ground or near ground measurements, any retrieval of PAR or fAPAR from RS platforms is mediated by a model, and the disagreement between currently available fAPAR products is high (Meroni et al., 2013; Pickett-Heaps et al., 2014). This fosters the implementation of a flexible and robust framework able to tackle these three issues concurrently, by means of an appropriate modeling of light interception, absorption and emission, and to eventually consistently retrieve Φ_F at canopy level from RS data. This parameter could offer an additional observational constraint on modeled carbon uptake (MacBean et al., 2018) independent of canopy structure and illumination conditions.

Physically-based Radiative Transfer Models (RTMs) of the vegetation have been used in the last decades to express mathematically the complex interactions between plant elements (*e.g.*, tissues, leaves, branches) and the electromagnetic radiation. RTMs inversion techniques have been widely used to retrieve vegetation parameters such as chlorophyll content (C_{ab}) or leaf area index (LAI) from RS data (for a review of methods and applications see Verrelst et al., 2015a), but so far few of them incorporated the F signal within the modeling or the retrieval process. The 1-D (vertical) "Soil-Canopy Observation Photosynthesis and Energy fluxes" (SCOPE) model (van der Tol et al., 2009) is a state of the art integrated radiative transfer and energy balance model that enables the simulation of canopy leaving hyperspectral reflectance and fluorescence, modeling the full radiative transfer of light from the photosystem to the top of canopy, as well as the turbulent heat fluxes and photosynthesis. van der Tol et al. (2016) successfully exploited high resolution (Spectral Sampling Interval (SSI) = 0.24 nm and Full Width at Half Maximum (FWHM) = 1 nm) top of canopy reflectance spectra in the visible and near-infrared (VNIR) spectral region, to partially invert SCOPE to retrieve biochemical and structural parameters of the vegetation (*e.g.*, pigment concentration, canopy structure), and further simulate emitted F_{760}. Very recently, Verhoef et al. (2018) developed a scheme based on several routines of SCOPE and a F retrieval based on principal components, to obtain F together with important vegetation parameters out of FLEX/Sentinel-3 top of atmosphere synthetic data. Verhoef et al. (2018) showed that it was possible to reach a remarkable accuracy, given the correct atmospheric characterization. Hernández-Clemente et al. (2017) extended a 3-D radiative transfer model to simulate F in complex canopies, and used this model (FluorFLIGHT) to account for the effects of sunlit/shadow pixels, vegetation structure and fractional cover on F in an oak forest, highlighting the importance of a proper modeling approach to relate F to forest health. Nevertheless, 3-D models are generally slower and require a larger number of input parameters than simpler 1-D RTMs, and this can be a limiting factor for their invertibility and their large-scale application.

In this work we propose a novel approach to improve the characterization of the physiological conditions of plants from hyperspectral RS data through the inversion of a light version of the SCOPE model. Compared to van der Tol et al. (2016) and to Verhoef et al. (2018), in this work we retrieve the full F spectrum and Φ_F as direct products of the numerical inversion of a physically based model. This work aims at using these, together with other important vegetation biochemical and biophysical parameters consistently retrieved within the inversion process, to assess vegetation status in a case of induced stress. In order to evaluate the proposed approach, we compare the retrieved F values with state of the art SFM and SpecFit algorithms (Cogliati et al., 2015) and we analyze the temporal evolution of the retrieved parameters during the controlled stress experiment. Finally, we compare the retrieved Φ_F values with an independent biochemical model of photosynthesis and fluorescence to sketch a conceptual use of Φ_F to inform on PQ.

2. Materials and methods

2.1. Experimental setup

The field campaign was conducted in a farm in Latisana (Udine, Italy; 13.013E, 45.779N) from 7th June 2014 to 3rd July 2014, during the ESA funded FLEX-EU campaign. Three parcels (9 m × 12 m) of a commercially produced lawn were treated with different doses of Dicuran 700 FW (Syngenta AG), a commercial formulation of Chlorotoluron (3-(3-chloro-p-tolyl)-1,1-dimethylurea). Chlorotoluron is an herbicide that interferes with the light reactions of photosynthesis, inhibiting the electron transport chain from photosystem II to photosystem I. This translates in a strong decrease of PQ, and in an accumulation of absorbed energy inside the reaction centers that has to be rapidly dissipated to avoid oxidative stress. Chlorotoluron is also known to inhibit NPQ, hence we expect a strong increase of Φ_F, driven by an increase in F emission, after the treatment. On the other hand, the vegetation biophysical and biochemical parameters should only be influenced at a later stage. Three additional non-treated plots were sprayed with water and used as control. A similar treatment was exploited in Rossini et al. (2015), with noticeable effects on both F_{687} and F_{760}. The lawn was frequently irrigated during the campaign and was expected to never experience water limited conditions. A preliminary assessment of the full dataset showed i) no differences between the control plots and ii) that the effect of the lower doses of Dicuran was statistically comparable. Hence, for the sake of simplicity, data shown in this paper refer only to three plots, representative of the more (maximum dose, 24 ml^{-1}) and less stressed (minimum dose, 1.5 ml^{-1}) among the treated plots, as well as a control plot. Due to logistic constraints, the herbicide was applied on the two plots seven days apart (12th June 2014 and 19th June 2014, respectively) hence in this paper the Day After the Treatment (DAT), instead of the Day Of the Year (DOY) will be used.

2.2. Top of canopy hyperspectral measurements

High resolution spectral measurements were performed in the field with three Ocean Optics (Dunedin, USA) portable spectrometers operating in the VNIR region with different spectral configurations (Table 1). The spectrometers were housed in a Peltier thermally regulated box (model NT-16, Magapor, Zaragoza, Spain) keeping the internal temperature at 25 °C in order to ensure the stability of both the intensity and the spectral information of the measured signal. The targets were measured from nadir with bare optical fibers (field of view of 25 °) at a distance of 1.30 m, yielding to an observed circular surface of approximately 0.58 m of diameter. The fibers were mounted down-looking on a specially modified tripod that allowed the alternate measurement of the vegetated target and of the white reference calibrated panel (Labsphere Inc., North Sutton, NH, USA). A picture of the overall spectroscopic measurements setup is reported in Fig. 1a. This system has been widely used in the last decade to provide consistent values of reflectance and fluorescence in different field campaigns, over a wide range of crops and natural vegetation (Rossini et al., 2016). The spectral data were acquired with a dedicated software (3S; Meroni and Colombo, 2009) and processed with a specifically developed IDL (ITTVIS IDL 7.1.1) application described in Meroni et al. (2011). Each acquisition consisted of three spectra recorded sequentially: L_{in}^{meas} measured over the calibrated white reference panel, L_{out}^{meas} over the target and L_{in}^{meas} again. The actual L_{in}^{meas} at the time of the target measurement was estimated by linear interpolation. The relative variation of the two L_{in}^{meas} measurements was used as a quality check for illumination condition stability (*i.e.*, total variation below 5%). Each of these spectra is the average of 10 and 3 scans (for the full range and the other two spectrometers, respectively) in order to reduce instrumental noise.

Fig. 1b shows a nadiral picture of one of the measured lawn parcel. A white frame was used as a reference to ensure spatially consistent measurements of the vegetated surface (depicted approximately with the yellow circle) over time. To ensure that the white frame had no effect on the measurements (*i.e.*, signal contamination due to adjacency effects), two consecutive measurements with and without the frame were compared, showing no significant differences in terms of reflectance and fluorescence (data not shown). Ground measurements were performed over the whole time window of the campaign. Measurements started around 10:00 AM until 16:00 PM, depending on the weather conditions. The plots were measured moving the instruments from the first to the last plot cyclically during the day. Five consecutive acquisitions were taken for each plot under stable illumination conditions before moving to the next one. The final spectral dataset consisted of ≈ 600 measurements. The spectra collected with the three spectrometers were converted from digital numbers to radiance and then merged together in order to cover the VNIR spectrum (400–900 nm) with the maximum possible spectral resolution (*i.e.*, minimum SSI and FWHM). In this work, in fact, in order to retrieve concurrently the biophysical parameters by model inversion technique, the F_{687} and F_{760} at the oxygen absorption bands, as well as the full spectrum F, the spectra collected with the highest spectral resolution spectrometers (S-O_2-B and S-O_2-A) were accurately inter-calibrated based on the lower resolution spectrometer (S-Full), and merged together to obtain a single spectrum with the highest possible resolution (Fig. 2). Top of canopy F was retrieved in the O_2-A and O_2-B oxygen absorption bands using state of the art spectral fitting methods (SFM; Cogliati et al., 2015), originally proposed by Meroni and Colombo (2006) and Meroni et al. (2010). This method models the fluorescence and the *true* reflectance (ρ^{SFM}; *i.e.*, the ratio of the reflected radiance and the incoming radiance) as a function of wavelengths inside the O_2-A and O_2-B oxygen absorption bands. F^{SFM} and ρ^{SFM} were modeled using Voigt functions and piecewise cubic splines, respectively. Moreover, the SpecFit algorithm as described in Cogliati et al. (2015) was applied to retrieve the full spectrum of the F emission ($F^{SpecFit}$) in the spectral range from 670 nm to 780 nm. The integral of each F spectrum ($F_{int}^{SpecFit}$) was computed by means of trapezoidal numerical integration.

Table 1
Summary of the technical characteristics of the Ocean Optics spectrometers (Dunedin, USA) used in the measurement campaign. "Range" is the spectral range, "SSI" is the Spectral Sampling Interval, "FWHM" is the Full Width at Half Maximum and "SNR" is the nominal Signal-to-Noise Ratio.

ID	Model	Range [nm]	SSI [nm]	FWHM [nm]	SNR
S-Full	HR4000	400–1000	0.24	1.00	300:1
S-O_2-B	QE65000	657–743	0.10	0.25	1000:1
S-O_2-A	HR4000	717–805	0.02	0.10	300:1

Starting from the measured radiance fluxes, the measured *apparent* reflectance ($\rho^{*,meas}$) was computed. $\rho^{*,meas}$ is a quantity defined as the ratio between the radiance leaving the vegetation surface (L_{out}^{meas}) and the incoming radiance (L_{in}^{meas}). It differs from the *true* reflectance (ρ) for including not only the reflected, but also the emitted radiance (*i.e.*, the fluorescence).

2.3. Modeling setup

2.3.1. Model description

The radiative transfer (RT) routines used to simulate reflectance and fluorescence were taken from the SCOPE model (version 1.70[1]). Four routines were selected for this purpose. At leaf level, reflectance and fluorescence spectra were simulated with a modified version of the Fluspect-B model (Verhoef, 2011; Vilfan et al., 2016), while for propagation through the canopy the routines RTMo for incident light and RTMf for fluorescence were used. Fluspect-B is based on the PROSPECT model (Jacquemoud and Baret, 1990), with the addition of backward and forward fluorescence spectra. Here, the absorption coefficients of leaf biochemical components from the recently published PROSPECT-D (Féret et al., 2017) were used. RTMo is based on the SAIL model (Verhoef, 1984), and it simulates the four-stream radiative transfer of the incident light, resulting in the reflectance. Finally, RTMf propagates the fluorescence fluxes simulated by Fluspect-B inside the canopy based on the distribution of APAR and the scattering coefficients modeled with RTMo. The soil reflectance was modeled using the "Global Soil Vector" (GSV) model (Jiang and Fang, 2012; Verhoef et al., 2014). The coupled model resulting from the combination of Fluspect-B, RTMo, RTMf and GSV is a "light" version of SCOPE, and it is referred to as "RTMc" in this study.

2.3.2. Model inversion

The model inversion routine for the retrieval of biophysical and biochemical parameters of the vegetation was based on a Numerical Optimization (NO) algorithm that minimizes the differences between the measured and the modeled apparent reflectance in the spectral region from 400 nm to 900 nm. The modeled apparent reflectance ($\rho^{*,RTM}$) is defined by the ratio of the modeled radiance leaving the vegetation surface (L_{out}^{RTM}) and the incoming radiance:

$$\rho^{*,RTM} = \frac{L_{refl}^{RTM} + F_{out}^{RTM}}{L_{in}^{meas}} = \frac{L_{out}^{RTM}}{L_{in}^{meas}} \quad (3)$$

where F_{out}^{RTM} is the modeled fluorescence in the observation direction, and the modeled reflected radiance (L_{refl}^{RTM}) is computed as:

$$L_{refl}^{RTM} = \frac{r_{so}(\pi L_{sun}^{meas}) + r_{do}(\pi L_{sky}^{meas})}{\pi} \quad (4)$$

where r_{so} and r_{do} are the canopy reflectance factors of the direct (solar) and diffuse (sky) components of the incoming irradiance (πL_{sun}^{meas} and

[1] https://github.com/Christiaanvandertol/SCOPE.git.

(a) (b)

Fig. 1. a) Picture of the spectroscopic setup in the field; b) Parcel of the measured lawn: the yellow circle is approximately the area measured with the spectroscopic system. (For interpretation of the references to color in this figure legend, the reader is referred to the web version of this article.)

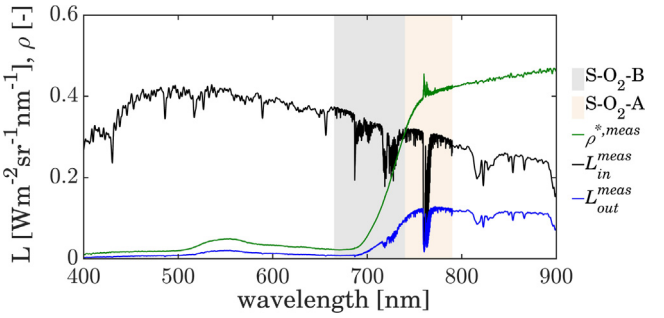

Fig. 2. Example of the spectra collected with the three spectrometers merged together to obtain the highest resolution spectral configuration. The shaded areas represent the regions where the data from the high resolution spectrometers (S-O_2-B and S-O_2-A) were used instead of the full-range one (S-Full). (For interpretation of the references to color in this figure, the reader is referred to the web version of this article.)

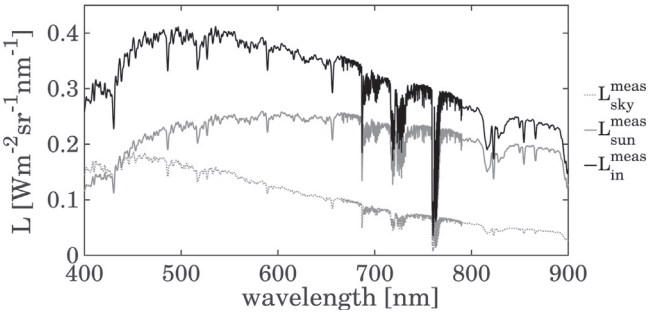

Fig. 3. Example of the measured total incoming radiance (L_{in}^{meas}) and the decomposed direct (L_{sun}^{meas}) and diffuse (L_{sky}^{meas}) fluxes.

πL_{sky}^{meas}, respectively). L_{sun}^{meas} and L_{sky}^{meas} were not directly measured in the field, but were obtained by decomposing L_{in}^{meas} according to a simulation produced with the MODerate resolution atmospheric TRANsmission (MODTRAN) RT model (Berk et al., 2014), so that the sum of the two components was equal to the measured total L_{in}^{meas} (Eq. (5)).

$$L_{in}^{meas} = L_{sun}^{meas} + L_{sky}^{meas} \quad (5)$$

Table 2
Lower boundaries (LB), upper boundaries (UB), *a priori* values (p_0), assumed standard deviations (σ_{p0}) and starting values (SV) of each retrieved parameter. Free parameters include six Fluspect-B parameters for Chlorophyll (C_{ab}) and carotenoids (C_{car}), dry matter (C_{dm}), water content (C_w), senescent material (C_s) and fluorescence quantum efficiency (*fqe*, equivalent to Φ_F), Leaf Area Index (*LAI*) from the SAIL model, and volumetric soil moisture percentage in the root zone (*SMp*) from the GSV model.

Parameter	Unit	LB	UB	p_0	σ_{p0}	SV
C_{ab}	μg cm^{-2}	0	100	40	30	40
C_{car}	μg cm^{-2}	0	30	10	10^9	10
C_{dm}	g cm^{-2}	0	0.04	0.01	10^9	0.005
C_w	cm	0	0.05	0.01	10^9	0.02
C_s	–	0	0.4	0.15	10^9	0.1
fqe (Φ_F)	–	0	1	0.01	10^9	0.01
LAI	m^2 m^{-2}	0	6	2	1	3
SMp	%	5	55	30	10^9	30

An example of the spectra obtained from this decomposition is shown in Fig. 3. Given a set of arbitrary starting model parameters (Table 2, column SV), the true Solar zenith and azimuth angles, and the L_{sun}^{meas} and L_{sky}^{meas} components, the NO algorithm iteratively executes the RTMc model, varying all the free parameters within their range of variation (Table 2), until a cost function is minimized.

A number of parameters were left free to vary during the inversion routine. In particular, six Fluspect-B parameters for Chlorophyll (C_{ab}) and carotenoid content (C_{car}), dry matter (C_{dm}), water content (C_w), senescent material (C_s), fluorescence quantum efficiency (*fqe*), and Leaf Area Index (*LAI*) from the SAIL model. *SMp* is a parameter in the GSV model for the volumetric soil moisture percentage in the root zone, and it was left free to account for potential variations in the soil brightness due to soil moisture content. The Fluspect-B parameter "*fqe*" corresponds to Φ_F. In order to test the retrieval scheme in a generally applicable configuration, the lower (Table 2, column LB) and upper boundaries (column UB) of the free parameters were left very wide. A spherical leaf angle distribution (LIDFa = −0.35; LIDFb = −0.15), was chosen to model the lawn canopy. It was left fixed because no variation in the canopy architecture was observed during the campaign.

Following van der Tol et al. (2016), we used the `lsqnonlin` function of the optimization toolbox in MATLAB® R2016b, selecting a Trust-Region-Reflective least squares algorithm for updating

parameters after each iteration step. The cost function "f" was defined as:

$$f = \mathrm{ER1}^{\mathrm{T}}\mathrm{ER1} + w^{*}\mathrm{ER2}^{\mathrm{T}}\mathrm{ER2}$$

$$\mathrm{ER1} = \begin{cases} \rho^{*,RTM}(\lambda) - \rho^{*,meas}(\lambda) & ,\lambda \in \lambda_{noabs} \\ (\rho^{*,RTM}(\lambda) - \rho_{BL}^{*,RTM}(\lambda)) + & ,\lambda \in \lambda_{abs} \\ \quad -(\rho^{*,meas}(\lambda) - \rho_{BL}^{*,meas}(\lambda)) & \end{cases}$$

$$\mathrm{ER2} = \frac{p - p_0}{\sigma_{p0}} \tag{6}$$

with λ_{abs} being the spectral ranges within the fluorescence emission region where major atmospheric absorption features occur, in particular:

- O_2-A from 754 nm to 775 nm
- O_2-B from 685 nm to 688 nm
- H_2O from 715 nm to 734 nm

and λ_{noabs} all other wavelengths in the 400–900 nm spectral range. The first term of the cost function (ER1) calculates the residuals between the modeled ($\rho^{*,RTM}$) and the measured apparent reflectance ($\rho^{*,meas}$). Outside the oxygen absorption bands, simply the difference between $\rho^{*,RTM}$ and $\rho^{*,meas}$ is used. However, inside the absorption bands, the apparent reflectance is normalized (subtracted) by a "baseline reflectance" (ρ_{BL}^{*}, the "baseline" of ρ^{*}). This ensures that the heights of the spikes in the apparent reflectance relative to the shoulders outside the absorption bands are reproduced rather than the absolute heights. This appears necessary as the $\rho^{*,RTM}$ may have some residual bias in the red-edge and the NIR plateau, which could strongly affect the retrieved fluorescence. ρ_{BL}^{*} is calculated by fitting a linear spline function to the ρ^{*} curve once the peaks due to F contribution are removed, an approach conceptually similar to the one used in the iFLD fluorescence retrieval (Alonso et al., 2008). ER1 in the absorption bands is then calculated as the difference of the modeled and measured residuals between ρ^{*} and ρ_{BL}^{*}. Fig. 4a shows an example of the minuend ($\rho^{*,meas} - \rho_{BL}^{*,meas}$) and the subtrahend ($\rho^{*,RTM} - \rho_{BL}^{*,RTM}$) of ER1 (Eq. (6)), in the spectral region around the O_2-A band, while in Fig. 4b ER1 computed for the whole dataset is compared to the difference between $\rho^{*,RTM}$ and $\rho^{*,meas}$. The second term (ER2) includes the posterior (p) and *a priori* (p_0) values of the model parameters, as well as their expected standard deviation (σ_p), weighted for a factor $w = 3 \times 10^{-2}$ (van der Tol et al., 2016). The output of this process is an optimized set of the input parameters, as well as the corresponding modeled reflectance and fluorescence spectra (Fig. 5). The integral of each F spectrum (F_{int}^{RTM}) was computed by means of trapezoidal numerical integration. In order to be consistent with the calculation of $F_{int}^{SpecFit}$, the spectral range was limited between 670 nm and 780 nm.

2.3.3. Evaluation of model inversion performance against synthetic data

In order to test the retrieval algorithms described in the previous section (*i.e.*, RTMc inversion, SFM and SpecFit), we created a large synthetic (> 800,000) look-up table of apparent reflectance spectra with RTMc, with the same spectral characteristics of the measured data. RTMc input parameters were varied over their whole range of variation (*i.e.*, the whole parameter space between LB and UB in Table 2), with a fixed-pass sampling ensuring at least five steps for each parameter. In addition, the short-wave incoming radiation (R_{in}) was varied between 400 and 1000 W m^{-2} with a 200 W m^{-2} step. A subset of randomly selected 1000 simulations was used to perform the inversion and to test the retrieval algorithms.

2.4. Regression models and error estimation

All data in the plots are reported as mean ± standard deviation, unless differently indicated. Similarly, the linear regression models

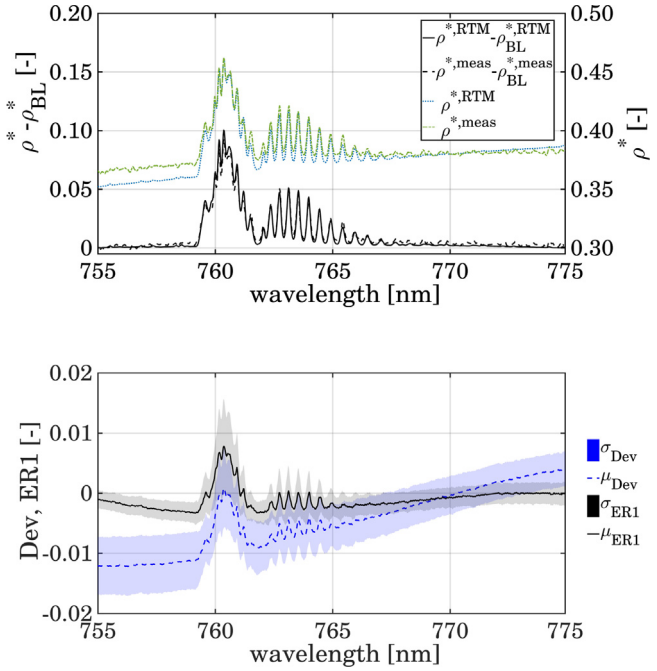

Fig. 4. a) Example of the minuend ($\rho^{*,meas} - \rho_{BL}^{*,meas}$) and the subtrahend ($\rho^{*,RTM} - \rho_{BL}^{*,RTM}$) of the term ER1 in the cost function (Eq. (6)), as well as the modeled ($\rho^{*,RTM}$) and measured ($\rho^{*,meas}$) apparent reflectance in the spectral region around the O_2-A band. b) Mean (μ) and standard deviation (σ) of the difference between $\rho^{*,RTM}$ and $\rho^{*,meas}$ (Dev) and of the ER1 term of the cost function, in the spectral region around the O_2-A band. Data in (b) refer to the whole dataset. (For interpretation of the references to color in this figure, the reader is referred to the web version of this article.)

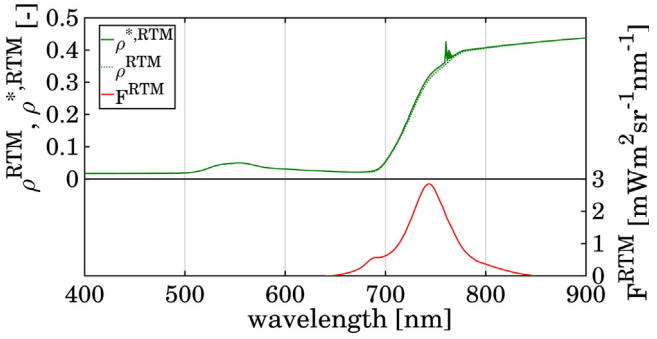

Fig. 5. Example of the true (ρ^{RTM}) and apparent ($\rho^{*,RTM}$) reflectance and fluorescence (F^{RTM}) spectra simulated with the RTMc model. (For interpretation of the references to color in this figure, the reader is referred to the web version of this article.)

shown in this paper are obtained with Ordinary Least Squares (OLS) fitting. For the robust regression models, the `bisquare` weighting scheme for downweighting outliers included in MATLAB® R2016b `fitlm` function was used.

The Root Mean Squared Error (RMSE) and the Relative Root Mean Squared Error (RRMSE) were computed according to Eqs. (7) and (8), respectively. Together with the slope (m), the intercept (q) and the coefficient of determination (R^2), they were used to compare the retrieved ($\hat{y}$) and the reference (y) values.

$$\mathrm{RMSE} = \sqrt{\frac{\sum_{i=1}^{n}(\hat{y}_i - y_i)^2}{n}} \tag{7}$$

Table 3
Coefficient of determination (R^2), Root Mean Square Error (RMSE), Relative Root Mean Square Error (RRMSE), slope (m) and intercept (q) of the OLS linear regression model between reference and retrieved values of RTMc parameters, fluorescence at 687 nm (F_{687}^{RTM}) and at 760 nm (F_{760}^{RTM}), as well as the integral of the full spectrum of F (F_{int}^{RTM}) are reported. Regression coefficients between reference values and F retrieved with SFM (F_{687}^{SFM} and F_{760}^{SFM}) and with SpecFit ($F_{int}^{SpecFit}$) starting from the simulated spectra are reported too. All values in brackets refer to the robust bisquare linear regression model. p-value is always < 0.001.

Parameter	Unit	R^2	RMSE	RRMSE [%]	m	q
C_{ab}	$\mu g\,cm^{-2}$	0.94 (0.99)	3.87 (1.19)	9.83 (3.02)	0.88 (0.91)	0.38 (0.00)
C_{car}	$\mu g\,cm^{-2}$	0.87 (0.98)	1.27 (0.57)	12.74 (5.70)	1.01 (1.04)	0.27 (0.01)
LAI	$m^2\,m^{-2}$	0.97 (0.97)	0.29 (0.26)	8.64 (7.75)	1.10 (1.13)	0.01 (−0.07)
fqe	–	0.95 (0.99)	0.004 (0.003)	10.38 (7.79)	1.34 (1.33)	0.004 (0.003)
F_{687}^{RTM}	$mW\,m^{-2}\,sr^{-1}\,nm^{-1}$	0.96 (0.99)	0.17 (0.12)	10.42 (7.36)	1.03 (1.02)	0.18 (0.13)
F_{760}^{RTM}	$mW\,m^{-2}\,sr^{-1}\,nm^{-1}$	0.95 (0.99)	0.95 (0.27)	8.67 (4.88)	0.99 (1.00)	0.59 (0.39)
F_{int}^{RTM}	$mW\,m^{-2}\,sr^{-1}$	0.96 (1.00)	41.26 (27.39)	8.31 (5.51)	1.00 (1.00)	55.08 (37.92)
F_{687}^{SFM}	$mW\,m^{-2}\,sr^{-1}\,nm^{-1}$	1.00 (1.00)	0.08 (0.03)	5.62 (2.11)	1.05 (1.02)	−0.01 (0.01)
F_{760}^{SFM}	$mW\,m^{-2}\,sr^{-1}\,nm^{-1}$	1.00 (1.00)	0.03 (0.03)	0.67 (0.67)	0.99 (0.99)	0.00 (−0.01)
$F_{int}^{SpecFit}$	$mW\,m^{-2}\,sr^{-1}$	0.99 (1.00)	36.70 (25.70)	8.49 (5.95)	1.01 (1.02)	0.90 (0.40)

$$RRMSE = \sqrt{\frac{\sum_{i=1}^{n}\left(\frac{\hat{y}_i - y_i}{y_i}\right)^2}{n}} * 100 \quad (8)$$

where n is the number of observations.

3. Results

3.1. Evaluation of the modeled reflectance and fluorescence

Table 3 shows the results of the inversion of the RTMc model on the synthetic spectral dataset. The comparison between fluorescence values at 687 nm (F_{687}^{RTM}) and at 760 nm (F_{760}^{RTM}) retrieved inverting RTMc and the reference values are reported as well. In general, the agreement between true and retrieved biochemical and biophysical vegetation parameters is good: the R^2 values are generally larger than 0.9 for most of the parameters, and the RMSEs are reasonably low. The slope of the OLS linear model for F_{687}^{RTM} and F_{760}^{RTM} are close to one, while there is a certain overestimation in retrieved F_{760}^{RTM} ($q = 0.59\,mW\,m^{-2}\,sr^{-1}\,nm^{-1}$). F^{RTM} values integrated over the whole emission spectrum (F_{int}^{RTM}) show similar R^2 value, with RMSE = $41.26\,mW\,m^{-2}\,sr^{-1}$ and $q = 55.08\,mW\,m^{-2}\,sr^{-1}$. The RRMSE is generally lower or very close to 10%.

When applying robust bisquare linear regression, the variance explained by the model is often close to 100%, and the RMSE is very low. Nevertheless, fqe is still overestimated ($m = 1.33$), and a positive bias in F_{760}^{RTM} and F_{int}^{RTM} values is still present ($q = 0.39\,mW\,m^{-2}\,sr^{-1}\,nm^{-1}$ and $q = 37.92\,mW\,m^{-2}\,sr^{-1}$, respectively). In order to evaluate the performances of the SFM and the SpecFit retrieval algorithms, F_{687}^{SFM} and F_{760}^{SFM} were retrieved starting from the simulated spectra, and the integral of the emitted fluorescence spectrum in the 670–780 nm spectral range was computed. If no additional noise is added to the simulated data, the agreement between the modeled (*i.e.*, the reference values in this case) and the retrieved F^{SFM} values is almost perfect (F_{687}^{SFM}: $R^2 = 1.00$, RMSE = $0.08\,mW\,m^{-2}\,sr^{-1}\,nm^{-1}$; F_{760}^{SFM}: $R^2 = 1.00$, RMSE = $0.03\,mW\,m^{-2}\,sr^{-1}\,nm^{-1}$; $F_{int}^{SpecFit}$: $R^2 = 1.00$, RMSE = $0.03\,mW\,m^{-2}\,sr^{-1}$), even though F_{687}^{SFM} values are slightly overestimated ($m = 1.05$). In all cases the RRMSE is lower than 10%, with a very low value of 0.67% for F_{760}^{SFM}, and these values further improve if robust bisquare linear regression models are used.

In this paragraph the results of the measured spectral dataset are reported. Fig. 6 shows an example of the measured ($\rho^{*,meas}$) and retrieved ($\rho^{*,RTM}$) apparent reflectance (left panel). The regions around the O_2-B and O_2-A oxygen absorption bands are highlighted. F_{687}^{SFM} and F_{760}^{SFM} values retrieved with SFM, the full F spectrum retrieved with SpecFit, as well as the F spectrum retrieved with RTMc (F^{RTM}) are reported. The deviation (difference) and the RRMSE between measured and retrieved apparent reflectance, computed for the whole dataset across the whole spectral range used for the model inversion, are shown in Fig. 7. In general the fitting is good, but the model systematically overestimates ρ^* in the blue region and it is not perfectly able to reproduce the slope of the red-edge and the NIR plateau. In particular, ρ^* is overestimated before 450 nm, from 700 nm to 745 nm, and from 770 nm to 835 nm, and it is underestimated afterwards. In the green region, from 500 nm to 550 nm, the model reproduced almost correctly the shape of the measured apparent reflectance, while small second order differences are still present.

The OLS linear regression model between F_{687}^{SFM} and F_{687}^{RTM} computed

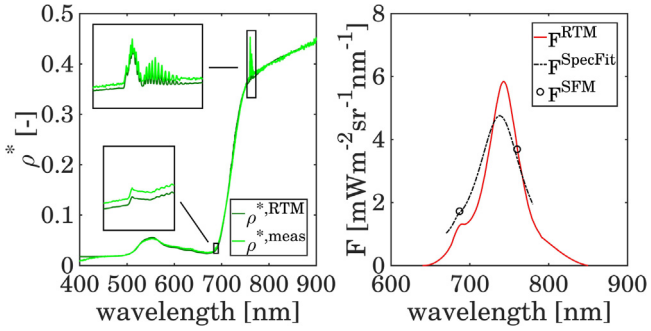

Fig. 6. Example of the measured and retrieved apparent reflectance (left) and fluorescence values (right). The regions around the O_2-B and O_2-A oxygen absorption bands are highlighted. (For interpretation of the references to color in this figure, the reader is referred to the web version of this article.)

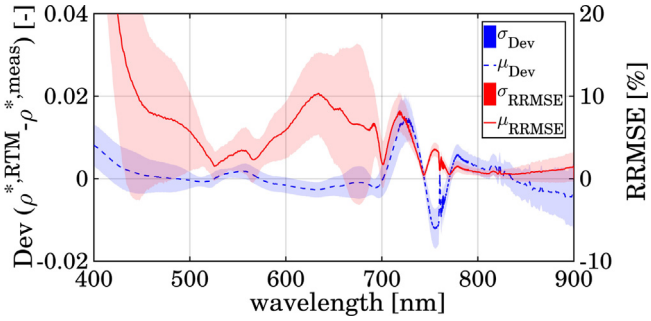

Fig. 7. Mean (μ) and standard deviation (σ) of the difference (Dev) and the Relative Root Mean Square Error (RRMSE) between measured and retrieved apparent reflectance (ρ^*), computed for the whole dataset across the whole spectral range used for the model inversion. (For interpretation of the references to color in this figure, the reader is referred to the web version of this article.)

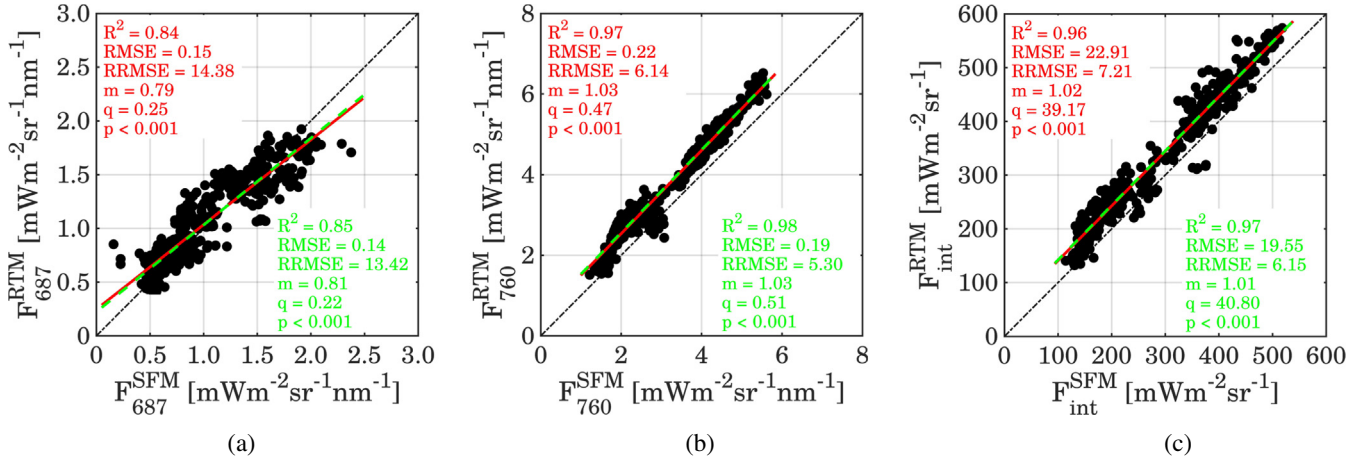

Fig. 8. OLS (red solid line) and robust bisquare linear regression model (green dashed line) between *F* values retrieved with SFM and obtained with RTMc inversion. a) Linear regression models for F_{687}; b) linear regression models for F_{760}; c) linear regression models for F_{int}. (For interpretation of the references to color in this figure legend, the reader is referred to the web version of this article.)

for the whole dataset of field measurements shows a good correlation between the two fluorescence retrievals ($R^2 = 0.84$) with a RMSE of $0.15\,mW\,m^{-2}\,sr^{-1}\,nm^{-1}$ (Fig. 8a). Two point clouds are clearly distinguishable, one composed by F_{687} values between $0.5\,mW\,m^{-2}\,sr^{-1}\,nm^{-1}$ and $1\,mW\,m^{-2}\,sr^{-1}\,nm^{-1}$, and the other composed by higher values. F_{760} (Fig. 8b) shows an even higher R^2 (0.97) and a slope much closer to 1 ($m = 1.03$), while the average RMSE is $0.22\,mW\,m^{-2}\,sr^{-1}\,nm^{-1}$. F_{int}^{RTMc} values (Fig. 8c) closely resemble $F_{int}^{SpecFit}$ ones ($m = 1.02$; $q = 39.17\,mW\,m^{-2}\,sr^{-1}$; $R^2 = 0.96$; RMSE = $22.91\,mW\,m^{-2}\,sr^{-1}$). When applying a robust bisquare linear regression model to the data (green dashed line), the fittings improve. In particular, the RMSE of F_{687} and F_{760} decreases to $0.14\,mW\,m^{-2}\,sr^{-1}\,nm^{-1}$ and $0.19\,mW\,m^{-2}\,sr^{-1}\,nm^{-1}$, respectively, while the R^2 slightly increases to 0.85 and 0.98. Nevertheless, the slope of the linear model for F_{687} is still far from one (m = 0.81) and the intercept (q) is $0.22\,mW\,m^{-2}\,sr^{-1}\,nm^{-1}$, while F_{760} from RTMc inversion is overestimated of about $0.51\,mW\,m^{-2}\,sr^{-1}\,nm^{-1}$.

3.2. Monitoring the retrieved parameters during the induced stress experiment

In this section the temporal evolution of a selection of parameters retrieved for the stress-detection field experiment, and the retrieved *F* radiances, are shown. In the following plots only data collected around solar noon, *i.e.*, ± 1 h, are used to compute mean and standard deviation for each DAT. Data refer to a control ("Control") and two treated plots, one with the lowest ("Low Dose") and the other with the highest dose in the experimental setup ("High Dose").

Modeled fluorescence values at the O_2-B (Fig. 9a) and O_2-A band (Fig. 9c) follow the dynamics observed in fluorescence retrieved with SFM quite well (Fig. 9b and d). Just after the treatment, there is an abrupt increase of both F_{760} and F_{687} and a subsequent decrease in the following days. The control plot shows no significant variation in *F* values over time. Absolute *F* values are correctly reproduced as well, coherently with what already shown in Section 3.1. Although there is a systematic overestimation of F_{int}^{RTM} values of about $40\,mW\,m^{-2}\,sr^{-1}$ compared to $F_{int}^{SpecFit}$, the relative agreement between the observed values is still high, and the temporal dynamics are preserved.

Fig. 10 shows the temporal variation of a selection of leaf and canopy retrieved parameters. A few hours after the treatment was applied, the relative variation of leaf chlorophyll content (C_{ab}; Fig. 10a) compared to the pre-treatment values was negligible. Starting from DAT 1, C_{ab} values of the treated plots started to decrease slowly. *LAI* values (Fig. 10b) in contrast were stable over time (as foreseen considering that the treatment did not induce any structural variation). During the campaign the grassland was not cut, thus a certain increase in plant biomass in the control plot could be easily justified. The content of senescent material (C_s; Fig. 10c) stays stable over time in both the control and the "Low Dose" plot, even though the average values differed almost by a factor of 2. In the "High Dose" plot, C_s increased over time following pigment degradation and plant browning. Retrieved Φ_F values (Fig. 10d) clearly show a quick and strong response of the photosynthetic apparatus to the applied treatment, even on DAT 0, few hours after the application. Φ_F values are in agreement with both F^{RTM} and F^{SFM} (in particular with F_{760} values).

3.3. Combined observation of Φ_F and C_{ab} for stress detection

Fig. 11 shows the combined variation of C_{ab} and Φ_F during the experiment for the three plots. In the control plot (Fig. 11a), Φ_F did not vary during the campaign, while there was a small fluctuation of C_{ab} values. Fig. 11b shows a circular pattern over time of Φ_F versus C_{ab}, after application of a low dose of Chlorotoluron ("Low Dose"). Immediately after the treatment, there was an abrupt rise of Φ_F with no variation of C_{ab}, while in the following three days, Φ_F values stayed high and C_{ab} started decreasing. From DAT 3 to 5, Φ_F and C_{ab} values decreased together, while from DAT 5 to 7 only Φ_F showed a further decrease. 14 days after the chemical was applied, values of both Φ_F and C_{ab} were close to the pre-treatment ones. On the other hand, when the treatment was applied with a much higher dose ("High Dose"; Fig. 11c), after a quick increase of Φ_F with almost no variation in C_{ab} values, both parameters started decreasing rapidly. Several days after the treatment, the plants were brownish, so that the measurements were stopped. At that point, almost 50% of the original C_{ab} content was lost, and the plants did not show any sign of recovery for the rest of the campaign.

4. Discussion

4.1. Monitoring vegetation dynamics through RTM inversion

Sun-induced fluorescence (*F*) has been shown to be a relevant proxy of photosynthetic activity at different scales. Nevertheless, due to the concurrent influence of multiple drivers on the remotely sensed *F* signal, it's unambiguous interpretation in the context of plant status analysis is still challenging. On the other hand, radiative transfer model inversion techniques have been increasingly used to retrieve quantitative information on vegetation parameters from hyperspectral remote sensing observations, but only few of them simulate the *F* signal. In this study, a state of the art radiative transfer model for reflectance and fluorescence was combined with very high resolution apparent

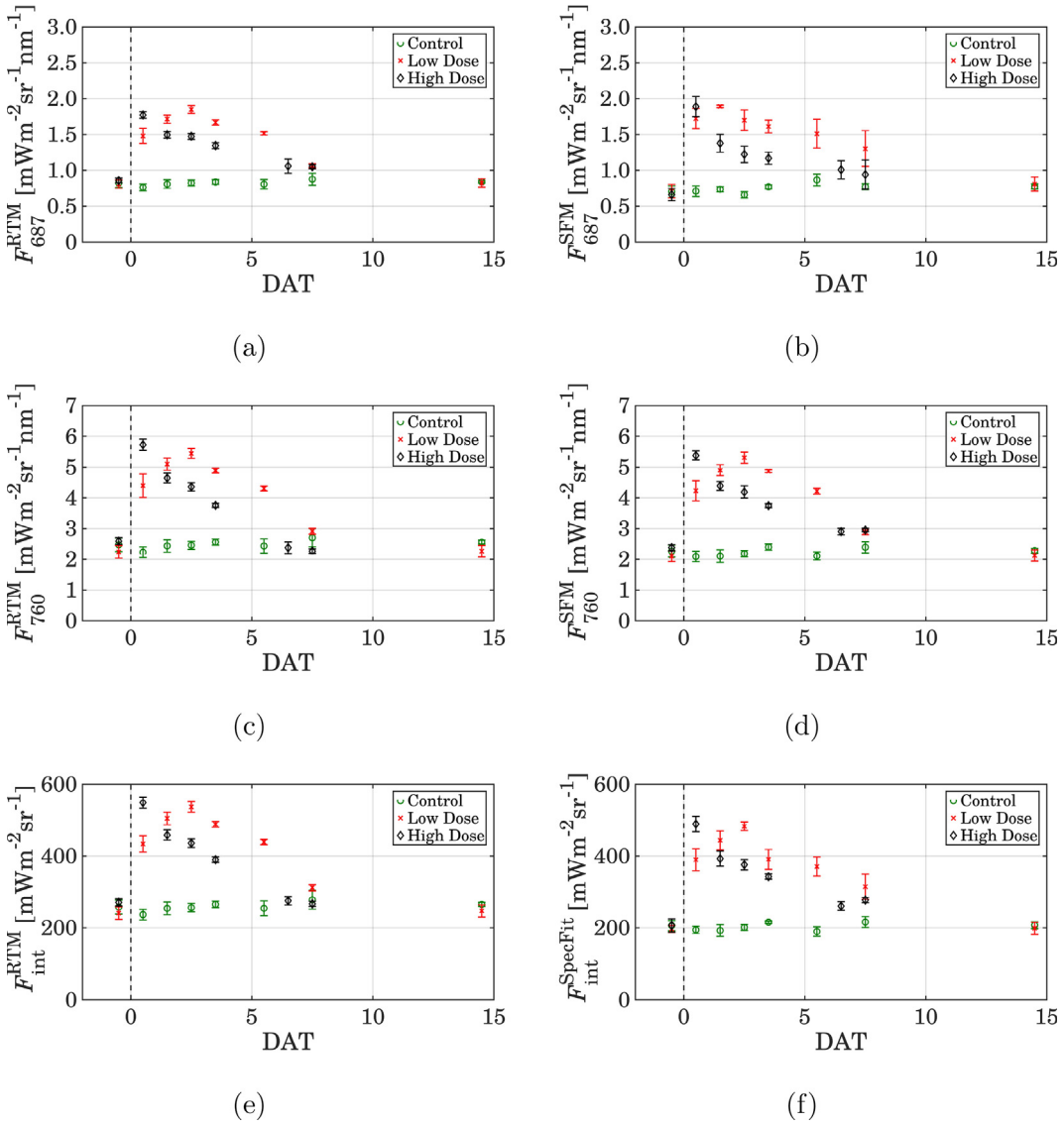

Fig. 9. Time series of fluorescence values retrieved with RTMc inversion ("a", "c" and "e") and with the SFM algorithm ("b", "d" and "f"). The x axis shows the number of Days After the Treatment (DAT).

reflectance spectra to retrieve coherent information about vegetation status and functioning. Typical hyperspectral VNIR measured spectra (FWHM ≈ 1 nm) and higher resolution measured spectra (FWHM ≈ 0.3 nm) in the fluorescence emission region were combined (merged in a single spectrum) to allow the consistent retrieval of both leaf/canopy biophysical parameters and F (and its quantum yield, Φ_F) based on model inversion through numerical optimization. This allowed to test the capability of the model in retrieving quantitatively and tracking over time very high variations in both fluorescence (full spectrum) and fluorescence quantum yield. This represents a different approach compared to previous studies, in which fluorescence was either produced with a look-up table approach (Hernández-Clemente et al., 2017), simulated in forward mode as a second step (van der Tol et al., 2016), or expressed as a function of modeled principal components (Verhoef et al., 2018). The retrieval approach proposed in our work fully exploits spectral observations as will be provided by FLEX, in which the broad range spectral information is combined with the very high spectral resolution radiance measurements at the oxygen absorption bands. Moreover, whereas van der Tol et al. (2016) and Hernández-Clemente et al. (2017) evaluated retrieved F values in the O_2-A band, we directly retrieved the full spectrum of fluorescence and its quantum yield during the numerical inversion process from apparent reflectance, and we compared it to state of the art SFM and SpecFit retrieval methods (Cogliati et al., 2015).

Very good agreement was found between the retrieved vegetation parameters and the reference values when testing the proposed model inversion framework on synthetic data (Table 3). Highly significant and very good relationships (p-value always < 0.001) were also obtained between RTMc-based and reference F values. These results indicate that the model inversion was able to effectively disentangle the effect of pigments and canopy structure on the apparent reflectance spectrum from the one due to F emission. This was possible thanks to: i) the inclusion of the modeling of F emission and its radiative transfer inside the leaf and the canopy within the forward model (RTMc); ii) the use of very high resolution apparent reflectance spectra in the VNIR spectral region; and iii) the specifically conceived cost function to invert RTMc (Eq. (6)).

When applying the retrieval scheme to the measured dataset, a very good agreement between measured and modeled spectral apparent reflectance was observed (Fig. 7). Nevertheless, there was a slight overestimation of ρ^* in the blue. This could be triggered by an underestimation of L_{sky}^{meas} (imperfect characterization of the atmospheric

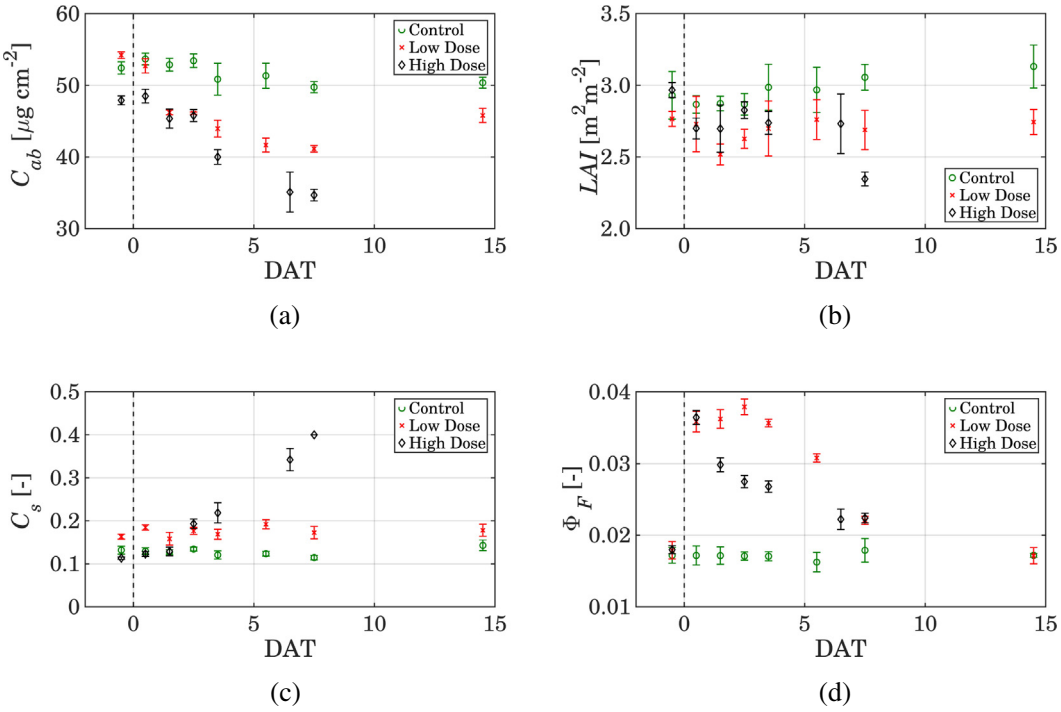

Fig. 10. Time series of parameters retrieved from RTMc inversion. The x axis shows the Day After Treatment (DAT).

scattering), due to the simplified accounting of the direct/diffuse ratio of the incoming radiation in the forward model. Apart from this aspect, within the context of this experiment uncertainties in the characterization of the direct and the diffuse components of the incoming radiation should have a very limited effect on the shape of the modeled reflectance outside the atmospheric absorption bands. The measurements, in fact, were always performed in cloud-free conditions, with Solar Zenith Angles (SZA) lower than 60°, and the real SZA was used to simulate the reflectance components in the model inversion routine. The fraction of direct/diffuse irradiance can nevertheless partly explain the residual difference in the modeling of apparent reflectance in the O_2-A band (750 nm to 770 nm). The depth of the absorption band depends on the path-length followed by photons from the sun via the target to the sensor (Cogliati et al., 2015), being therefore influenced by the direct/diffuse ratio. This is true for the O_2-B band as well, but its depth and width are lower compared to the O_2-A band, therefore this effect is less pronounced.

The remaining discrepancies in ρ^* could be partially attributed to the pigment absorption coefficients (cfr. van der Tol et al., 2016), especially in the green and red spectral regions. The discrepancy in the red-edge region, and in particular from 700 nm to 770 nm is likely due to the effect of an inaccurate retrieval of the senescent material in the leaves (C_s), a parameter that preferentially affects the slope of the reflectance in this spectral region. As an example, Fig. 12 shows the variation induced in the reflectance spectra when selectively varying C_s from 0 to 0.25, highlighting its strong selective impact over the green and the red edge. Although the mismatch in the modeled reflectance in this region could potentially translate into an uncertainty in the retrieved pigments, a very good agreement was found between a well-known vegetation index computed from the measured apparent reflectance related to the canopy chlorophyll content (*i.e.*, the MTCI; Dash and Curran, 2004) and the correspondent retrieved parameters ($R^2 = 0.86$; $p < 0.001$).

Applying SFM and SpecFit to the simulated spectra confirms what was observed in Cogliati et al. (2015), indicating that both are very good performing fluorescence retrieval algorithms when a proper estimation of the incoming solar irradiance is provided. In this work, in fact, the incoming radiation was directly measured at top of canopy

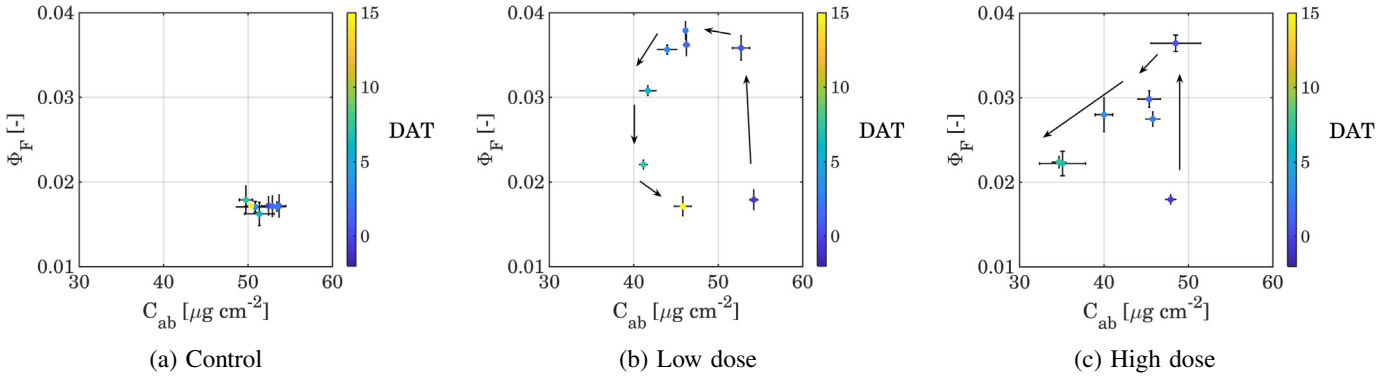

Fig. 11. Scatter plots between chlorophyll content (C_{ab}) and fluorescence yield (Φ_F), for three different plots: a control (panel "a"), a plot treated with a low dose ("b") and one with a high dose of herbicide ("c"). The color palette refers to the number of Days After the Treatment (DAT), the arrows follow the temporal dynamic as well. (For interpretation of the references to color in this figure legend, the reader is referred to the web version of this article.)

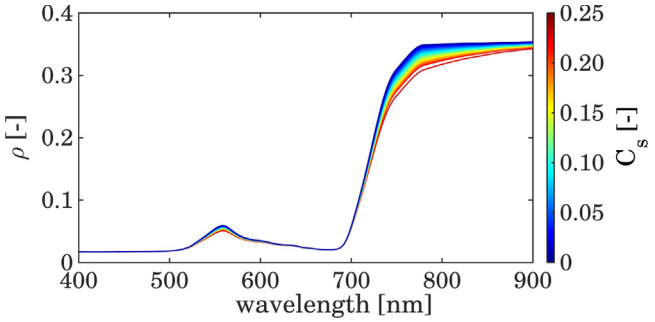

Fig. 12. Reflectance simulated with SCOPE 1.70 varying the content of senescent material in the leaves (C_s) from 0 to 0.25.

during the field campaign, and no atmospheric modeling was needed. There was a strong and consistent agreement between F values retrieved with RTMc inversion and SFM/SpecFit (Fig. 8). It is worth noting that the two fluorescence retrievals are completely independent and use different parametrization of the functions describing both fluorescence and reflectance. In this perspective, and lacking an independent reference for F values, RMSE and RRMSE are to be interpreted as "deviations" more than "errors". Moreover, due to the herbicide application, the range of variation of F_{760} and F_{687} found in this study is extreme when compared to what has been observed with the same measurement setup over a wide range of crops and natural vegetation (Rossini et al., 2016). This indicates that both SFM/SpecFit and the SCOPE-based RTMc model are flexible enough to cope with different (up to extreme) variations in emitted F triggered by stress events. Nevertheless, there is a bias in F_{int}^{RTM} that can be attributed to the different shape of the fluorescence emission spectrum modeled by the two algorithms (see Fig. 6). In particular, RTMc based F spectra tend to systematically overestimate F in the far-red region (cfr. Fig. 8b), and this triggers the overestimation in F_{int} as well. In this experiment the strongest driver of F variation is the inhibition of PQ and NPQ by the chemical application, this meaning that in this specific case the informative content of F and Φ_F is similar (in particular when looking only at midday measurements). This is consistent with what was observed in a recent study by Hernández-Clemente et al. (2017) using a dataset simulated with the 3-D FluorFLIGHT model (in particular cfr. Fig. 11d), that found a strong and linear correlation between far-red fluorescence and the model-based fluorescence quantum efficiency.

The promising results obtained in this study open interesting perspectives for exploiting the increasing number of high resolution data from multi-scale remote sensing (RS) platforms. Computational times could be shortened by means of emulators of the radiative transfer models (Rivera et al., 2015). Moreover, a multi-step inversion routine where computationally efficient retrieval algorithms would be used to retrieve key parameters like chlorophyll content (C_{ab}) and Leaf Area Index (LAI), then used as priors for a better regularization of the numerical optimization inversion scheme is already in development. In addition, in an operational perspective independently retrieved F values (*e.g.*, with SFM or SpecFit), could be used as a constrain inside the cost function as well, while in this study we used them as a benchmark for the modeled values. The proposed technique could be further implemented for remote sensing airborne (*e.g.*, HyPlant; Rascher et al., 2015) and satellite measurements (*e.g.*, FLEX), but in these cases a proper correction of the atmospheric effect must be included. Several efforts are ongoing in the FLEX community to develop robust algorithms that take advantage of the multi-sensor tandem mission FLEX/Sentinel-3 observations (Sabater et al., 2017) to atmospherically correct the remote observations, or to include the atmospheric modeling within the inversion scheme (Verhoef et al., 2018).

4.2. Comparison of the retrieved Φ_F values with an independent biochemical model

We have already discussed that Φ_F is linked to the activity of the photosynthetic machinery, so that a variation in the Photochemical (PQ) or Non-Photochemical Quenching (NPQ) reflects in a variation of Φ_F. According to Butler (1978), Φ_F can be expressed as a ratio of rate coefficients (K) (Eq. (9)):

$$\Phi_F = \frac{K_F}{K_F + K_D + K_N + K_P} \tag{9}$$

where K_F, K_D, K_N and K_P are the rate coefficients for fluorescence, constitutive thermal dissipation, NPQ and PQ, respectively. With $K_F = 0.05$ and $K_D = 0.95K_F = 0.05$ and $K_D = 0.95$ (van der Tol et al., 2014), Φ_F is maximum when both K_P and K_N are 0 (*i.e.*, both PQ and NPQ are blocked), so that $\Phi_F^{max} = 0.05/1 = 0.05$, and minimum when K_P and K_N are high (*e.g.*, 4, van der Tol et al., 2014), so that $\Phi_F^{min} = 0.05/9 \approx 0.005$, or when K_N is very high (*e.g.*, $K_N = 10$ and $K_P = 1$, Porcar-Castell et al., 2012), so that $\Phi_F^{min} = 0.05/12 \approx 0.001$. With unstressed (control) values around 0.015 and maximum stressed (treated) values around 0.035–0.040, the Φ_F values retrieved from the apparent reflectance through RTMc inversion span over most of the physiological range of Φ_F, up to values close to its maximum, which is as expected considering that the Chlorotoluron is known to strongly inhibit both PQ and NPQ. As a test, setting $K_P = 0.15$ and $K_N = 0.15$ in Eq. (9), the resulting Φ_F value of 0.039 indicates that even a small amount of residual (*i.e.*, non inhibited) PQ and NPQ would be enough to justify the retrieved maximum values of Φ_F. Although these results are promising and strengthen the reliability of the retrieved Φ_F values, it is worth noting that the stressor applied in this study is not representative for natural conditions, in which variations in NPQ are much more important and PQ is not artificially blocked. More efforts are needed in this direction, especially in enlarging the domain of the biochemical models to account for a wider range of physiological conditions, and in finding a proper regularization strategy for NPQ.

5. Conclusions

In this work we demonstrated that it is possible to quantitatively retrieve the full spectrum of emitted F, the main vegetation parameters that control light absorption and reabsorption inside the canopy, as well as a physiologically relevant parameter such as the quantum yield of fluorescence (Φ_F), by inverting numerically a light version of the SCOPE model on measured apparent reflectance spectra. We also demonstrated that the combined observation of these parameters over time led to the recognition of specific patterns of stress adaptation and stress recovery in a controlled experiment.

Using Φ_F (or F) to derive quantitative information about plant photosynthesis is still challenging. First results presented in this study are promising, and foster the use of repeated hyperspectral remote sensing observations together with radiative transfer and biochemical vegetation models for a better quantification of photosynthesis from space.

Acknowledgments

Data presented in this contribution were acquired in the framework of the FLEX-EU campaign funded by ESA (Contract No. 4000107143/12/NL/FF/lf, CCN2). The inversion routine was developed during a Short-Term Scientific Mission (COST-STSM-ES1309-36163) conducted by M.C. at the University of Twente, Faculty of Geo-Information Science and Earth Observation (ITC), The Netherlands, supported by the COST Action ES1309/OPTIMISE. P.Y. was supported by a China Scholarship Council grant (201406040058). The authors gratefully thank Radoslaw

Juszczak for his support during the STSM, Dirk Schüttemeyer, Chiara Cilia, Anke Schickling, Giorgio Alberti, Gemini delle Vedove, Karolina Sakowska, Marcin Strozecki, Radoslaw Juszczak and Marin Tudoroiu for their help during the field campaign and Mirco Migliavacca, Wouter Verhoef, Nastassia Vilfan and Giulia Tagliabue for their valuable comments on the model inversion scheme.

References

Alonso, L., Gómez-Chova, L., Vila-Francés, J., Amorós-López, J., Guanter, L., Calpe, J., Moreno, J., 2008. Improved fraunhofer line discrimination method for vegetation fluorescence quantification. IEEE Geosci. Remote Sens. Lett. 5 (4), 620–624.

Berk, A., Conforti, P., Kennett, R., Perkins, T., Hawes, F., van den Bosch, J., 2014. MODTRAN6: A Major Upgrade of the MODTRAN Radiative Transfer Code. SPIE Defense+ Security 9088, 90880H–90880H-7.

Butler, W.L., 1978. In the photochemical apparatus of photosynthesis. Ann. Rev. Plant Physiol. 29 (1), 345–378.

Cogliati, S., Verhoef, W., Kraft, S., Sabater, N., Alonso, L., Moreno, J., Rascher, U., Drusch, M., Colombo, R., 2016. Spectrum Fitting - A Potential Fluorescence Retrieval for the FLEX Mission. presented at European Space Agency Living Planet Symposium, 9-13 May 2016, Prague, Czech Republic.

Cogliati, S., Verhoef, W., Kraft, S., Sabater, N., Alonso, L., Vicent, J., Moreno, J., Drusch, M., Colombo, R., 2015. Retrieval of sun-induced fluorescence using advanced spectral fitting methods. Remote Sens. Environ. 169, 344–357.

Damm, A., Elbers, J., Erler, A., Gioli, B., Hamdi, K., Hutjes, R., Kosvancova, M., Meroni, M., Miglietta, F., Moersch, A., Moreno, J., Schickling, A., Sonnenschein, R., Udelhoven, T., Van Der Linden, S., Hostert, P., Rascher, U., 2010. Remote sensing of sun-induced fluorescence to improve modeling of diurnal courses of gross primary production (GPP). Glob. Chang. Biol. 16 (1), 171–186 1.

Dash, J., Curran, P.J., 2004. The MERIS terrestrial chlorophyll index. Int. J. Remote Sens. 25 (23), 5403–5413.

Drusch, M., Moreno, J., Del Bello, U., Franco, R., Goulas, Y., Huth, A., Kraft, S., Middleton, E.M., Miglietta, F., Mohammed, G., Nedbal, L., Rascher, U., Schüttemeyer, D., Verhoef, W., 2017. Concept – ESA ' s Earth Explorer 8. IEEE Trans. Geosci. Remote Sens. 55 (3), 1273–1284.

Féret, J.B., Gitelson, A.A., Noble, S.D., Jacquemoud, S., 2017. PROSPECT-D: towards modeling leaf optical properties through a complete lifecycle. Remote Sens. Environ. 193, 204–215.

Garbulsky, M.F., Peñuelas, J., Papale, D., Ardö, J., Goulden, M.L., Kiely, G., Richardson, A.D., Rotenberg, E., Veenendaal, E.M., Filella, I., 2010. Patterns and controls of the variability of radiation use efficiency and primary productivity across terrestrial ecosystems. Glob. Ecol. Biogeogr. 19 (2), 253–267.

Garzonio, R., Di Mauro, B., Colombo, R., Cogliati, S., 2017. Surface reflectance and sun-induced fluorescence spectroscopy measurements using a small hyperspectral UAS. Remote Sens. 9 (5), 472 may.

Gitelson, A.A., Gamon, J.A., 2015. The need for a common basis for defining light-use efficiency: implications for productivity estimation. Remote Sens. Environ. 156, 196–201.

Guanter, L., Aben, I., Tol, P., Krijger, J.M., Hollstein, A., Köhler, P., Damm, A., Joiner, J., Frankenberg, C., Landgraf, J., 2015. Potential of the TROPOspheric Monitoring Instrument (TROPOMI) onboard the Sentinel-5 precursor for the monitoring of terrestrial chlorophyll fluorescence. Atmos. Meas. Tech. 8 (3), 1337–1352.

Guanter, L., Alonso, L., Gómez-Chova, L., Meroni, M., Preusker, R., Fischer, J., Moreno, J., 2010. Developments for vegetation fluorescence retrieval from spaceborne high-resolution spectrometry in the O2-A and O2-B absorption bands. J. Geophys. Res.-Atmos. 115 (19) 10.

Guanter, L., Zhang, Y., Jung, M., Joiner, J., Voigt, M., Berry, J.A., Frankenberg, C., Huete, A.R., Zarco-Tejada, P., Lee, J.-E., Moran, M.S., Ponce-Campos, G., Beer, C., Camps-Valls, G., Buchmann, N., Gianelle, D., Klumpp, K., Cescatti, A., Baker, J.M., Griffis, T.J., 2014. Global and time-resolved monitoring of crop photosynthesis with chlorophyll fluorescence. Proc. Natl. Acad. Sci. U. S. A. 111 (14), E1327–E1333.

Hernández-Clemente, R., North, P., Hornero, A., Zarco-Tejada, P., 2017. Assessing the effects of forest health on sun-induced chlorophyll fluorescence using the FluorFLIGHT 3-D radiative transfer model to account for forest structure. Remote Sens. Environ. 193, 165–179.

Jacquemoud, S., Baret, F., 1990. PROSPECT: a model of leaf optical properties spectra. Remote Sens. Environ. 34 (2), 75–91.

Jiang, C., Fang, H., 2012. Soil Reflectance Modeling With a Global Spectral Library: Refinement of the Price Soil Reflectance Model. Presented at American Geophysical Union, Fall Meeting, 3-7 December 2012, San Francisco, CA, USA.

Joiner, J., Yoshida, Y., Guanter, L., Middleton, E.M., 2016. New methods for the retrieval of chlorophyll red fluorescence from hyperspectral satellite instruments: simulations and application to GOME-2 and SCIAMACHY. Atmos. Meas. Tech. 9 (8), 3939–3967.

Lee, J.-E., Frankenberg, C., van der Tol, C., Berry, J.A., Guanter, L., Boyce, K., Fisher, J.B., Morrow, E., Worden, J.R., Asefi, S., Badgley, G., Saatchi, S., 2013. Forest productivity and water stress in Amazonia: observations from GOSAT chlorophyll fluorescence forest productivity and water stress in Amazonia: observations from GOSAT chlorophyll fluorescence. Proc. R. Soc. Lond. B Biol. Sci. 280 (1761).

Liu, X., Liu, L., Zhang, S., Zhou, X., 2015. New spectral fitting method for full-spectrum solar-induced chlorophyll fluorescence retrieval based on principal components analysis. Remote Sens. 7 (8), 10626–10645.

MacBean, N., Maignan, F., Bacour, C., Lewis, P., Peylin, P., Guanter, L., Köhler, P., Gómez-Dans, J., Disney, M., 2018. Strong constraint on modelled global carbon uptake using solar-induced chlorophyll fluorescence data. Sci. Rep. 8 (1), 1–12.

Meroni, M., Atzberger, C., Vancutsem, C., Gobron, N., Baret, F., Lacaze, R., Eerens, H., Leo, O., 2013. Evaluation of agreement between space remote sensing SPOT-VEGETATION fAPAR time series. IEEE Trans. Geosci. Remote Sens. 51 (4), 1951–1962.

Meroni, M., Barducci, A., Cogliati, S., Castagnoli, F., Rossini, M., Busetto, L., Migliavacca, M., Cremonese, E., Galvagno, M., Colombo, R., Morra di Cella, U., 2011. The hyperspectral irradiometer, a new instrument for long-term and unattended field spectroscopy measurements. Rev. Sci. Inst. 82 (4), 1–10.

Meroni, M., Busetto, L., Colombo, R., Guanter, L., Moreno, J., Verhoef, W., 2010. Performance of spectral fitting methods for vegetation fluorescence quantification. Remote Sens. Environ. 114 (2), 363–374 2.

Meroni, M., Colombo, R., 2006. Leaf level detection of solar induced chlorophyll fluorescence by means of a subnanometer resolution spectroradiometer. Remote Sens. Envir. 103 (4), 438–448 8.

Meroni, M., Colombo, R., 2009. 3S: a novel program for field spectroscopy. Comput. Geosci. 35 (7), 1491–1496 7.

Meroni, M., Rossini, M., Guanter, L., Alonso, L., Rascher, U., Colombo, R., Moreno, J., 2009. Remote sensing of solar-induced chlorophyll fluorescence: review of methods and applications. Remote Sens. Environ. 113 (10), 2037–2051 10.

Monteith, J.L., 1972. Solar radiation and productivity in tropical ecosystems. J. Appl. Ecol. 9 (3), 747–766.

Pickett-Heaps, C.A., Canadell, J.G., Briggs, P.R., Gobron, N., Haverd, V., Paget, M.J., Pinty, B., Raupach, M.R., 2014. Evaluation of six satellite-derived fraction of absorbed photosynthetic active radiation (FAPAR) products across the Australian continent. Remote Sens. Environ. 140, 241–256.

Porcar-Castell, A., Garcia-Plazaola, J.I., Nichol, C.J., Kolari, P., Olascoaga, B., Kuusinen, N., Fernández-Marín, B., Pulkkinen, M., Juurola, E., Nikinmaa, E., 2012. Physiology of the seasonal relationship between the photochemical reflectance index and photosynthetic light use efficiency. Oecologia 170 (2), 313–323.

Porcar-Castell, A., Tyystjärvi, E., Atherton, J., van der Tol, C., Flexas, J., Pfündel, E.E., Moreno, J., Frankenberg, C., Berry, J.A., 2014. Linking chlorophyll a fluorescence to photosynthesis for remote sensing applications: mechanisms and challenges. Journal of experimental botany 65 (15), 4065–4095 8.

Rascher, U., Alonso, L., Burkart, A., Cilia, C., Cogliati, S., Colombo, R., Damm, A., Drusch, M., Guanter, L., Hanus, J., Hyvärinen, T., Julitta, T., Jussila, J., Kataja, K., Kokkalis, P., Kraft, S., Kraska, T., Matveeva, M., Moreno, J., Muller, O., Panigada, C., Pikl, M., Pinto, F., Prey, L., Pude, R., Rossini, M., Schickling, A., Schurr, U., Schüttemeyer, D., Verrelst, J., Zemek, F., 2015. Sun-induced fluorescence - a new probe of photosynthesis: first maps from the imaging spectrometer HyPlant. Glob. Chang. Biol. 21 (12), 4673–4684.

Rivera, J.P., Verrelst, J., Gómez-Dans, J., Muñoz-Marí, J., Moreno, J., Camps-Valls, G., 2015. An emulator toolbox to approximate radiative transfer models with statistical learning. Remote Sens. 7 (7), 9347–9370.

Rossini, M., Meroni, M., Celesti, M., Cogliati, S., Julitta, T., Panigada, C., Rascher, U., van der Tol, C., Colombo, R., 2016. Analysis of red and far-red sun-induced chlorophyll fluorescence and their ratio in different canopies based on observed and modeled data. Remote Sens. 8 (5), 412.

Rossini, M., Nedbal, L., Guanter, L., Ač, A., Alonso, L., Burkart, A., Cogliati, S., Colombo, R., Damm, A., Drusch, M., Hanus, J., Janoutova, R., Julitta, T., Kokkalis, P., Moreno, J., Novotny, J., Panigada, C., Pinto, F., Schickling, A., Schüttemeyer, D., Zemek, F., Rascher, U., 2015. Red and far red Sun-induced chlorophyll fluorescence as a measure of plant photosynthesis. Geophys. Res. Lett. 42 (6), 1–8.

Sabater, N., Alonso, L., Cogliati, S., Vicent, J., Tenjo, C., Verrelst, J., Moreno, J., 2015. A sun-induced vegetation fluorescence retrieval method from top of atmosphere radiance for the FLEX/Sentinel-3 TanDEM mission. In: 2015 IEEE International Geoscience and Remote Sensing Symposium (IGARSS), pp. 2669–2672 7.

Sabater, N., Vicent, J., Alonso, L., Cogliati, S., Verrelst, J., Moreno, J., 2017. Impact of atmospheric inversion effects on solar-induced chlorophyll fluorescence: exploitation of the apparent reflectance as a quality indicator. Remote Sens. 9 (6), 1–20.

van der Tol, C., Berry, J.A., Campbell, P.K.E., Rascher, U., 2014. Models of fluorescence and photosynthesis for interpreting measurements of solar-induced chlorophyll fluorescence. J. Geophys. Res.: Biogeosci. 119 12.

van der Tol, C., Rossini, M., Rascher, U., Verhoef, W., Mohammed, G., 2016. A model and measurement comparison of diurnal cycles of sun induced chlorophyll fluorescence of crops. Remote Sens. Environ. 186 (iii), 1–13.

van der Tol, C., Verhoef, W., Timmermans, J., Verhoef, A., Su, Z., 2009. An integrated model of soil-canopy spectral radiances, photosynthesis, fluorescence, temperature and energy balance. Biogeosciences 6 (12), 3109–3129.

Verhoef, W., 1984. Light scattering by leaf layers with application to canopy reflectance modeling: the SAIL model. Remote Sens. Environ. 16, 125–141.

Verhoef, W., 2011. Modelling vegetation fluorescence observations: abstract. In: 7th EARSEL workshop of the Special Interest Group in imaging spectroscopy : final programme, 11-13 April 2011, Edinburgh, UK. pp. 41–42.

Verhoef, W., van der Tol, C., Middleton, E.M., 2014. Vegetation canopy fluorescence and reflectance retrieval by model inversion using optimization. In: 5th International Workshop on Remote Sensing of Vegetation Fluorescence. 1. pp. 759–770.

Verhoef, W., van der Tol, C., Middleton, E.M., 2018. Hyperspectral radiative transfer modeling to explore the combined retrieval of biophysical parameters and canopy fluorescence from FLEX - Sentinel-3 tandem mission multi-sensor data. Remote Sens. Environ. 204 (October 2017), 942–963.

Verrelst, J., Camps-Valls, G., Muñoz-Marí, J., Rivera, J.P., Veroustraete, F., Clevers, J.G., Moreno, J., 2015a. Optical remote sensing and the retrieval of terrestrial vegetation bio-geophysical properties - a review. ISPRS J. Photogramm. Remote Sens. 108, 273–290.

Verrelst, J., Rivera, J.P., van der Tol, C., Magnani, F., Mohammed, G., Moreno, J., 2015b.

Global sensitivity analysis of the SCOPE model: what drives simulated canopy-leaving sun-induced fluorescence? Remote Sens. Environ. 166, 8–21.
Vilfan, N., van der Tol, C., Muller, O., Rascher, U., Verhoef, W., 2016. Fluspect-B: a model for leaf fluorescence, reflectance and transmittance spectra. Remote Sens. Environ. 186, 596–615.
Yang, X., Tang, J., Mustard, J.F., Lee, J.-e., Rossini, M., Joiner, J., Munger, J.W., Kornfeld, A., Richardson, A.D., 2015. Solar-induced chlorophyll fluorescence that correlates with canopy photosynthesis on diurnal and seasonal scales in a temperate deciduous forest. Geophys. Res. Lett. (42), 2977–2987.
Zarco-Tejada, P.J., Suarez, L., Gonzalez-Dugo, V., 2013. Spatial resolution effects on chlorophyll fluorescence retrieval in a heterogeneous canopy using hyperspectral imagery and radiative transfer simulation. IEEE Geosci. Remote Sens. Lett. 10 (4), 937–941.
Zhao, F., Guo, Y., Verhoef, W., Gu, X., Liu, L., Yang, G., 2014. A method to reconstruct the solar-induced canopy fluorescence spectrum from hyperspectral measurements. Remote Sens. 6, 10171–10192.